LANGMUIR

pubs.acs.org/Langmuir Article

Wicking in Paper-Based Devices with Engineered Surface Grooves

Bhargav Rallabandi,* Sidharth Modha, Brent Kalish, and Hideaki Tsutsui*

Cite This: *Langmuir* 2025, 41, 34292−34298 Read Online

ACCESS | Metrics & More | Article Recommendations

ABSTRACT: Wicking of fluid in paper-based microfluidic devices can be greatly enhanced by engineering macroscopic grooves into the surface of the paper. We developed a quantitative model of this enhancement by resolving the coupled flow in the paper matrix and the groove. While the groove enhances wicking by providing a low-resistance conduit for flow, we find that the degree of enhancement depends strongly on the poorer wettability of the groove as well as the effect of gravity. We obtain an analytical prediction of imbibed length as a function of time, generalizing the Lucas−Washburn law to microporous wicks with engineered macroscopic surface grooves. The prediction is shown to be in quantitative agreement with previous experiments of upward wicking in both single- and multigrooved paper channels. The model also rationalizes the experimental finding that wide grooves may slow down imbibition despite their larger cross-sectional area and, thus, identifies optimal groove widths.

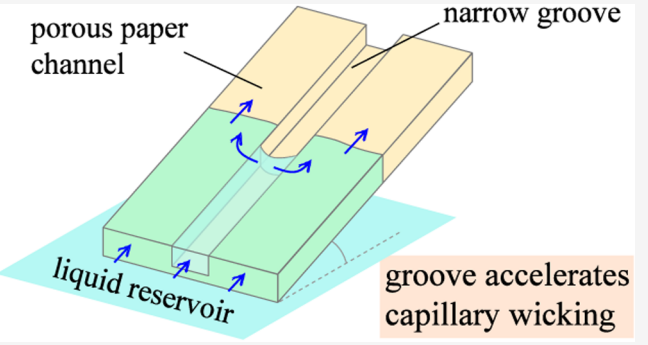

INTRODUCTION

Paper-based microfluidic devices have undergone substantial development since their resurgence in 2007,[1] driven by their ease of fabrication, low-cost materials, user-friendly operation, and versatility as a sensing platform.[2,3] These devices operate by using capillary forces to wick fluid and analytes through the pore spaces of a thin strip of paper. The simplest devices involve predominantly one-dimensional flow with simple enzymatic and colorimetric reactions at the end[1] or along the length of a strip.[4] However, devices require more sophisticated fluid handling to perform more complex chemical reactions, necessary for increased sensitivity, and to target a wider range of analytes. For example, the enzyme-linked immunosorbent assay (ELISA) involves sequential deliveries of the sample, reagents, and a wash buffer at timed intervals to maximize the detection signal while minimizing the background noise.[5] These chemistries often require repeated manual intervention. Automating these steps necessitates a quantitative understanding and control of fluid flow in paper.

Capillary imbibition in porous media, such as paper, is classically described by the Lucas−Washburn (LW) equation,[6] which models the paper as a bundle of capillary tubes of some effective diameter. The model balances the driving capillary pressure with viscous resistance to flow, predicting that the location of the fluid front grows with the square root of the time. Although the LW framework is simple to use, it does not fully capture the complexities of many practical paper microfluidic devices, motivating the development of more detailed models that address the effects of evaporation and ambient relative humidity,[7−9] non-uniform channel geometries,[10−13] swelling fibers,[14−16] multiple layers of paper,[17−20] and even backing materials.[21−23] Other work, focusing on model porous media, has studied the effects of inertia and contact-angle dynamics,[24] the role of open versus closed channels,[25,26] and the wicking of non-Newtonian[27] and multiphase[28] fluids.

Of particular interest to this work is imbibition in multiscale porous media, which comprise a microporous matrix that contains larger macroporous features. Examples in the context of paper microfluidics include multi-ply paper channels separated by macroporous gaps[17−20] as well as paper channels with grooves cut along their length.[29−31] These systems exhibit faster wicking than in unmodified paper channels due to the lower hydraulic resistance of the macroporous features, presenting opportunities for flow control. To understand these behaviors, models based on an area-averaged LW law[17] and resistor networks,[32] which weigh the effective diameters of the paper matrix and gap, have been proposed. While these approaches offer an explanation of accelerated wicking in horizontal channels, they overpredict wicking rates in vertical multi-ply devices as well as grooved paper channels. A

Received: August 14, 2025
Revised: November 18, 2025
Accepted: November 18, 2025
Published: December 17, 2025

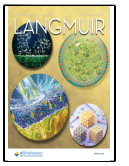

significant theoretical advance for multi-ply channels is due to Schaumburg and Berli,[19] who recognized that gravity limits wicking in the macroporous gap, even though it is negligible within the microporous matrix. Their modeling framework couples the flows in the gap and the matrix, resulting in a nonlinear system of equations that was solved numerically.

We build on the advances of Schaumburg and Berli,[19] generalizing it to grooved channels and developing new physical insight. We show that, in practical systems, the coupled system of equations governing the flow at the microporous (paper matrix) and macroporous (groove) scales reduces to an analytical prediction for the location of the fluid front as a function of time. This generalizes the LW law to multiscale porous media, accounting for gravity, the inclination angle, and the effect of the groove. The theory recovers previous experimental data for upward wicking with single and multiple grooves, including the observation that the rate of wicking depends non-monotonically on the groove width. We also show that, with a negative angle, the introduction of a groove can lead to wicking that is linear in time, beating the LW behavior. The simplicity of the main theoretical result is expected to provide a useful framework for the design of microfluidic devices that can be further adapted to more complex configurations.

MODEL

We consider the imbibition of liquid into a strip of porous material (paper), into which a narrow groove is etched by removing material (Figure 1). The front and back faces of the grooved paper strip are either exposed to the atmosphere or are covered by an impermeable backing material (such as an adhesive tape) as is common in paper-based microfluidic devices to provide structural stability and minimize evaporation.[21−23] The strip of paper has width w_p and thickness d_p and is characterized by pores of typical radius r_p occupying a volume fraction ϕ. The groove has width w_g and depth $d_g \le d_p$. The base of the strip is introduced to a reservoir of liquid (density ρ and viscosity μ) at an angle α relative to the horizontal, causing the liquid to wick into the porous matrix and the groove.

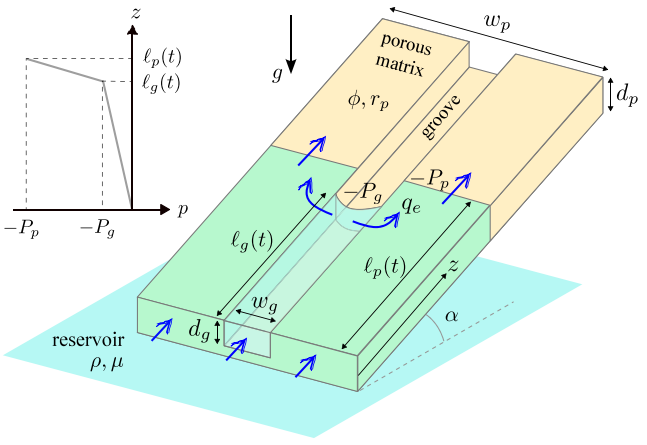

Figure 1. A strip of paper with a narrow groove running through its length wicks liquid from a reservoir. The front and back surfaces of the paper are either exposed to air or may be covered by an impermeable backing material.

The imbibed liquid column lengths in the groove and paper matrix are $l_{p,g}(t)$. Surface tension γ at the curved air−liquid interfaces produces capillary pressures $-P_{p,g} = -2\gamma\kappa_{p,g}$, where $\kappa_{p,g}$ is the mean curvature of the meniscus in the respective medium. Note that $\kappa_p \propto r_p^{-1}$, while $\kappa_g \propto w_g^{-1}$ or d_g^{-1}; therefore, $P_p \gg P_g$ for the practically relevant case of small pores. Consequently, the liquid in the paper matrix leads to the liquid in the groove ($l_p > l_g$) after initial transients. The opposite situation would entail a meniscus with a greater negative pressure (in the paper matrix) lagging behind a meniscus with a less negative pressure (in the groove). Such a configuration is dynamically unstable and would rapidly equilibrate with the one shown in Figure 1.

In most applications, the imbibed lengths are much longer than the width or thickness of the paper. Then, the fluid pressure varies primarily along the length of the paper (z), while variations across the width and thickness of the paper strip are small. The inertia of the flow in the microporous paper is negligible; therefore, the flow in the paper matrix is governed by Darcy's law, with permeability $k_p \propto r_p^2$. The liquid level in the groove grows like $l_g \propto \sqrt{t}$ at early times (Figure 2), so that, in typical experiments, the Reynolds number in the groove, $Re_g = \rho w(dl_g/dt)/\mu$ falls below unity for $t \gtrsim 0.5$ s. Thus, on time scales of interest in experiments (a few minutes), the liquid column in the groove is slender ($l_g/w_g \ll 1$) and inertia is negligible $Re_g \ll 1$. Under these conditions, the flow in the groove is quasi-parallel, so that the area-averaged z velocity in the groove is also governed by an effective Darcy's law with permeability k_g that depends on its cross-sectional geometry.[33]

Accounting for gravity, the area-averaged longitudinal velocity in either medium, $v_{p,g}$, is governed by

$$v_{p,g} = -\frac{k_{p,g}}{\mu}\left(\frac{\partial p}{\partial z} - \rho g \sin\alpha\right) \tag{1}$$

where $p(z,t)$ is the pressure; note that gravity resists flow for $\alpha > 0$. The volumetric fluxes in the paper and the groove are $\phi A_p v_p$ and $A_g v_g$, respectively, where $A_g = w_g d_g$ and $A_p = w_p d_p - w_g d_g$ are the cross-sectional areas of the two media. The total volumetric fluid flux is therefore $q = v_g A_g + \phi v_p A_p$ in the region $z < l_g$ (both the paper and the groove are wet) and $q = \phi v_p A_p$ for $l_g < z < l_p$ (only the paper is wet). Mass conservation demands that q does not vary with z; therefore, we conclude from eq 1 that $\partial p/\partial z$ is a constant in each region. With enforcement of the atmospheric pressure at the reservoir and capillary pressures at the two menisci, we find that the pressure distribution is

$$p(z,t) = \begin{cases} -P_g \dfrac{z}{l_g}, & 0 < z < l_g \\ -P_g - (P_p - P_g)\dfrac{z - l_g}{l_p - l_g}, & l_g < z < l_p \end{cases} \tag{2}$$

The pressure distribution predicted by eq 2 is sketched in Figure 1, and it indicates that the pressure gradient $\partial p/\partial z$ is discontinuous at $z = l_g$. Consequently, the flux in the paper matrix, $\phi A_p v_p$, is smaller when $z < l_g$ (smaller pressure gradient) and becomes larger for $z > l_g$ (larger pressure gradient). The jump in flux in the paper across $z = l_g$ is

$$q_e = [\phi A_p v_p]_{z=l_g^-}^{z=l_g^+} = \frac{\phi A_p k_p}{\mu}\left(\frac{P_p - P_g}{l_p - l_g} - \frac{P_g}{l_g}\right) \tag{3}$$

This excess flux occurs because fluid is entrained from the groove into the paper at $z = l_g$ due to the greater (negative) capillary pressure in the porous matrix. Mass conservation in the groove requires that flux at the groove's meniscus equals the flux entering the groove from the reservoir minus the flux lost to the paper, leading to the velocity at the groove meniscus $dl_g/dt = v_g|_{z=l_g} = v_g|_{z=0} - q_e/A_g$. The velocity at the paper meniscus is straightforward, $dl_p/dt = v_p|_{z=l_p}$. Using eqs 1 and 2, these relations yield a coupled pair of nonlinear differential equations for the imbibed lengths in the porous matrix and the groove

$$\frac{dl_p}{dt} = \frac{k_p}{\mu}\left(\frac{P_p - P_g}{l_p - l_g} - \rho g \sin\alpha\right) \tag{4a}$$

https://doi.org/10.1021/acs.langmuir.5c04278
Langmuir 2025, 41, 34292−34298

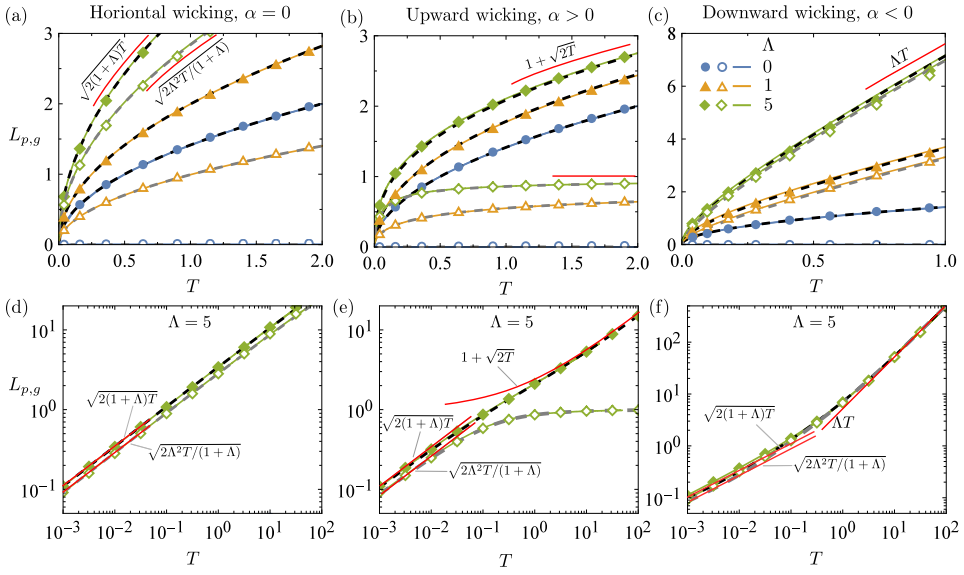

Figure 2. Evolution of $L_p(T)$ and $L_g(T)$ for different Λ from numerical solutions of eq 6 with $\mathcal{K} = 100$ (symbols), the implicit solution (eq 11) (solid curves), and the approximation (eq 12) (dashed curves). The legend indicated in panel c applies to all panels. Closed (open) symbols represent L_p (L_g). (a and d) Horizontal wicking ($\alpha = 0$). The liquid length in the paper and the groove grow like $L_p \sim \sqrt{2(1+\Lambda)T}$ and $L_g \sim \sqrt{2\Lambda^2 T/(1+\Lambda)}$. (b and e) Upward wicking ($\alpha > 0$). At long times, the liquid length in the groove saturates ($L_g \sim 1$), while the length in the paper grows as $L_p \sim 1 + \sqrt{2T}$. (c and f) Downward wicking ($\alpha < 0$). The liquid length in both the groove and the paper grow linearly in time as $L_{p,g} \sim \Lambda T$. Panels d–f show the data for $\Lambda = 5$ on logarithmic axes, indicating behaviors at long and short times.

$$\frac{\mathrm{d}l_g}{\mathrm{d}t} = \frac{k_g}{\mu}\left(\frac{P_g}{l_g} - \rho g \sin\alpha\right) - \frac{\phi A_p k_p}{\mu A_g}\left(\frac{P_p - P_g}{l_p - l_g} - \frac{P_g}{l_g}\right) \tag{4b}$$

The paper wicks fluid from both the reservoir and the groove, while the groove wicks fluid from the reservoir and loses some of it to the paper.

For typical microfluidic applications involving centimeter-scale imbibition lengths, the capillary pressure in the paper matrix is much greater than the hydrostatic pressure due to the small pores of the paper. Gravity in eq 4a serves to establish the capillary rise height in the paper, but this is so large (several meters) that it is irrelevant in paper-based microfluidics. However, gravity may be important in the groove, whose capillary pressure is much smaller than that in the paper ($P_g \ll P_p$). In particular, the capillary rise height in groove $\propto P_g/(\rho g)$ can be on the order of a centimeter, which is within the range relevant to practical microfluidics. We therefore neglect gravity in eq 4a while retaining it in eq 4b and also approximate $P_p - P_g \approx P_p$.

With these approximations, we recover the model of Schaumburg and Berli.[19] While those authors solved the coupled system numerically, we find new insights here by developing an analytical theory. We first observe that the hydrostatic pressure becomes comparable to the capillary pressure in the groove at a characteristic length, $l_c = P_g/|\rho g \sin\alpha|$ (for $\alpha > 0$, l_c is the capillary rise height in the groove). The characteristic time to wick this length through the paper matrix is $t_c = \mu l_c^2/(k_p P_p) = \mu P_g^2/(\rho^2 g^2 k_p P_p \sin^2\alpha)$. We use these scales to define dimensionless time and liquid column lengths (uppercase)

$$T = \frac{t}{t_c} = \frac{t\rho^2 g^2 k_p P_p \sin^2\alpha}{\mu P_g^2} \tag{5a}$$

and

$$L_{p,g} = \frac{l_{p,g}}{l_c} = \frac{\rho g|\sin\alpha| l_{p,g}}{P_g} \tag{5b}$$

Then, the rescaled form of eq 4 is

$$\frac{\mathrm{d}L_p}{\mathrm{d}T} = \frac{1}{L_p - L_g} \tag{6a}$$

$$\frac{1}{\mathcal{K}}\frac{\mathrm{d}L_g}{\mathrm{d}T} = \frac{1}{L_g} - \Gamma - \frac{1}{\Lambda}\left(\frac{1}{L_p - L_g}\right) \tag{6b}$$

where

$$\mathcal{K} = \frac{k_g P_g}{k_p P_p}, \quad \Lambda = \frac{A_g k_g P_g}{\phi A_p k_p P_p}, \quad \text{and} \quad \Gamma = \mathrm{sgn}(\sin\alpha) \tag{7}$$

are dimensionless parameters. Here, $\mathcal{K}$ is a ratio of characteristic flow velocities in the groove and the paper, and Λ is the ratio of volumetric fluxes. The parameter Γ captures the effect of gravity: it is +1 when the wicking is upward ($\alpha > 0$), −1 when it is downward ($\alpha < 0$), and 0 when it is horizontal. For a groove of roughly square cross-section, the capillary pressures are $P_p \propto \gamma/r_p$ and $P_g \propto \gamma/w_g$, while the permeabilities are $k_p \propto r_p^2$ and $k_g \propto w_g^2$. Then, the velocity ratio $\mathcal{K} \propto w_g/r_p$ is large, while the flux ratio $\Lambda \sim w_g^2/(\phi r_p w_p)$ is moderate due to the combination of a highly permeable but narrow groove and a less permeable but wider porous matrix. For a millimeter-wide strip of paper with micrometer-size pores and a 100 μm wide groove, we estimate $\mathcal{K} = O(100)$ and Λ between 1 and 10. The characteristic length l_c is a centimeter, while the characteristic wicking time t_c is about 30 s.

Enhanced Lucas–Washburn Law for Grooved Paper Channels. In the practically relevant limit of $\mathcal{K} \gg 1$, the left-hand side of eq 6b, $\mathcal{K}^{-1}(\mathrm{d}L_g/\mathrm{d}T)$, becomes negligible. Thus, almost all of the fluid drawn from the reservoir by the groove is quasi-statically lost to the paper matrix due to the extremely high permeability of the groove. This reduces eq 6b to an algebraic equation, which relates L_g to L_p by

$$L_g \simeq \frac{U + 2\Lambda - \sqrt{U^2 + 4\Lambda}}{2\Lambda\Gamma} \tag{8}$$

where we have defined

https://doi.org/10.1021/acs.langmuir.5c04278
Langmuir 2025, 41, 34292−34298

$$U(T) = 1 + \Lambda(\Gamma L_p(T) - 1) \tag{9}$$

Substituting the above result with eq 6a produces a single differential equation for $U(T)$

$$\frac{dU}{dT} = \frac{2\Gamma^2\Lambda^2}{\sqrt{U^2 + 4\Lambda} + U - 2} \tag{10}$$

We solve eq 10 with the initial condition $L_p|_{T=0} = 0$ (equivalently, $U|_{T=0} = 1 - \Lambda$) to obtain an implicit solution for the time T in terms of U

$$T = \frac{1}{4\Gamma^2\Lambda^2}\left((U-2)^2 - 2(\Lambda+1) + U\sqrt{U^2+4\Lambda} + 4\Lambda \log\left[\frac{\sqrt{U^2+4\Lambda}+U}{2}\right]\right) \tag{11}$$

which relates T to both L_g and L_p through eqs 8 and 9.

To develop an explicit solution of the form $L_{p,g}(T)$, it is necessary to invert the transcendental eq 11. To this end, we analyze eq 11 separately at early times (T, $L_{p,g} \ll 1$) and late times (T, $L_{p,g} \gg 1$) and construct a generalized Padé approximant that captures both limits. This procedure yields

$$L_p(T) \simeq \begin{cases} \dfrac{\sqrt{2(\Lambda+1)T} + 2(\sqrt{\Lambda+1}-1)T}{1 + (\sqrt{\Lambda+1}-1)\sqrt{2T}}, & \alpha > 0 \\ \sqrt{2(\Lambda+1)T}, & \alpha \to 0 \\ \dfrac{(1+2\Lambda^2 T)\sqrt{2(\Lambda+1)T} + \Lambda T}{1 + 2\Lambda\sqrt{2(\Lambda+1)T}} + \dfrac{3}{2}\log(1 + (\Lambda T)^{2/3}), & \alpha < 0 \end{cases} \tag{12}$$

Analogous expressions for $L_g(T)$ are then obtained by using the above results in eq 9 to find U and then substituting into eq 8. The relations eqs 11 and 12 represent the key results of this work. In particular, eq 12 is a generalization of the LW law that accounts for the entrainment of fluid between a macroporous groove and a microporous matrix, including the effects of gravity.

RESULTS AND DISCUSSION

Model Results. We test the theory by numerically solving eq 6. As predicted by the theory, we find that the results of the numerical solutions are insensitive to the specific choice of $\mathcal{K}$ since $\mathcal{K} \gg 1$; we use $\mathcal{K} = 100$ throughout. Figure 2 shows the time evolution of L_g and L_p for a few different values of Λ and for horizontal, upward, and downward wicking. The wicking dynamics predicted by the analytic solution (eq 11) and its approximation (eq 12) are nearly indistinguishable from each other and from numerical solutions across all T and Λ.

To understand the wicking behaviors, we first recall that Λ represents the relative importance of the groove. In the absence of a groove ($\Lambda = 0$), the wicking follows the classical LW law $L_p = \sqrt{2T}$ or $l_p = \sqrt{2D_0 t}$, where $D_0 = k_p P_p/\mu$ is the LW mobility in the paper matrix. In this regime, the wicking is not affected by α since gravity is negligible in the pores of the paper. The introduction of a groove accelerates the imbibition. During the initial stages of wicking, the imbibed liquid columns are short; therefore, gravity plays a negligible role. At these early times, we find a LW-type imbibition $l_p = \sqrt{2Dt}$ [or $L_p \sim \sqrt{2(\Lambda+1)T}$] with an enhanced mobility $D = D_0(1+\Lambda)$ due to the groove (Figure 2a). This enhanced wicking is a consequence of the fluid simultaneously entering the paper matrix from the groove and the reservoir.

When the wicking is horizontal, this enhanced LW behavior persists at all times. Gravity becomes important at long times for non-horizontal configurations. When the wicking is upward ($\alpha > 0$), the hydrostatic pressure in the groove opposes wicking; therefore, the liquid level in the groove saturates at $l_g = P_g/(\rho g \sin\alpha)$ (or $L_g \sim 1$). However, the groove continues to imbibe fluid from the reservoir and continually feeds it to the porous matrix. Consequently, wicking in the paper follows an offset version of the LW law of bare paper $l_p \sim P_g/(\rho g \sin\alpha) + \sqrt{2D_0 t}$ (or $L_p \sim 1 + \sqrt{2T}$); see Figure 2b. The stationary column in the groove now becomes the primary liquid source for the paper.

Gravity plays a much more important role when the wicking is downward (Figure 2c). It now aids the flow, driving the liquid level in the groove to advance linearly in time. The groove feeds the paper matrix as before, leading to $L_{p,g} \sim \rho g k_g \sin\alpha A_g t/(\phi A_p \mu)$ (or $L_{p,g} \sim \Lambda T$). The rate of growth differs from that of an isolated groove by a factor of $A_g/(\phi A_p)$, which occurs because the growing liquid column in the groove is spread across the area of the paper matrix. In contrast with the horizontal and upward cases, downward wicking leads to linear imbibition at long times, beating classical LW growth. This linear growth occurs solely due to contact with the groove, despite the negligible gravitational forces in the pores of the paper.

When the paper's cross-sectional area becomes very small, the groove dominates the wicking and negligible liquid is entrained into the porous matrix. This corresponds to $\Lambda \gg \mathcal{K} \gg 1$ and is not directly relevant to typical paper microfluidic devices. While this regime is outside the range of validity of eq 12, the coupled system (eq 6) indeed recovers the groove-only regime in the appropriate limit ($\Lambda \to \infty$).

Comparison to Experiments. We compare the theoretical predictions to experiments of upward vertical wicking ($\alpha = 90°$) from our previous study.[31] In that study, straight grooves were fabricated on Whatman grade 4 filter paper strips by using an Epilog Zing 16 CO_2 laser cutter. Grooves of 180 μm width were made by cutting a line element, while their depth was controlled by the laser's traverse speed. Wider grooves were created by cutting rectangular boxes instead. The fabricated paper devices were mounted vertically in a humidity-controlled chamber (99% RH; therefore, evaporation effects are negligible), and wicked deionized water was placed in a reservoir. The imbibed distances in the paper matrix were recorded over time by using a Nikon D5100 camera.

To compare the present theory to these experiments, we relate permeabilities and capillary pressures to the relevant physical and geometric properties of the system. We adopt the simplest approach of modeling the paper as a bundle of capillaries with effective radius r, which yields a Darcy permeability $k_p = r^2/8$ and a capillary pressure $P_p = (2\gamma\cos\theta)/r$, where θ is the contact angle of the air−water interface with paper. The effective permeability of a rectangular groove can be expressed as $k_g = w_g d_g f(w_g/d_g)$, where f is a known function of the aspect ratio.[33] To determine P_g, we denote the contact angles at the front, back, and side faces of the groove by θ_f, θ_b, and θ_s, respectively. An infinitesimal displacement dz of the meniscus in the groove changes the interfacial energy by $\gamma(\cos\theta_f + \cos\theta_b)w_g dz + 2\gamma\cos\theta_s d_g dz$, which is compensated

https://doi.org/10.1021/acs.langmuir.5c04278
Langmuir 2025, 41, 34292−34298

by the work done by the capillary pressure, $P_g w_g d_g dz$. This leads to[19,34]

$$P_g = \gamma\left(\frac{2\cos\theta_s}{w_g} + \frac{\cos\theta_f + \cos\theta_b}{d_g}\right) \quad (13)$$

We expect θ to be close to 0° since the porous paper matrix is highly wetting, whereas $0° < \theta_s < 90°$ since the laser etching burns the side faces of the groove, lowering its wettability. The contact angles θ_f and θ_b depend on whether the groove is cut all the way through the paper as well as the choice of backing material. They are expected to be close to or even exceed 90° since the front and back faces are more hydrophobic than the surfaces exposed to the paper matrix. These features make the groove less wettable than the paper matrix. Whether the groove is open or closed on the front and back surface also affects the boundary conditions and the shape of the meniscus, impacting both k_g and P_g.[25,26] In the interest of simplicity, we do not account for these detailed features here but rather capture their effect on fluid fluxes through the contact angles, which we treat as free parameters when we compare to experiments. As noted earlier, inertia is negligible over the time scales of interest in the experiments. The capillary number $\mu v/\gamma$ is small ($\lesssim 10^{-4}$); therefore, we treat the contact angles as constants throughout the wicking dynamics.

Single Groove: Effect of the Width. To determine the various parameters in theory, we first calibrate the properties of the paper matrix with a wicking experiment in a bare (ungrooved) paper strip (Figure 3a). The experimental data in this section correspond to the "no tape" data in Figure 4b of Modha et al.,[31] where the groove is cut through the thickness of the paper and no backing materials are applied, leaving the front and back faces of the channel open to the atmosphere. For ungrooved paper ($\Lambda = 0$), eq 12 retrieves the classical LW law $l_p = \sqrt{2D_0 t}$, with $D_0 = k_p P_p/\mu = \gamma r_p \cos\theta/(4\mu)$. The $l_p(t)$ data in ungrooved paper closely follow the LW law with $D_0 \approx 6.4$ mm^2/s, leading to $r_p \cos\theta \approx 0.51$ μm. The closeness of this fit also confirms that gravity plays a negligible role in the pores of the paper.

The introduction of a groove ($w_g = 180$ μm) accelerates the wicking, as has been reported in past studies. The early-time behavior follows a LW law $l_p \sim \sqrt{2D_{early} t}$, with $D_{early} \approx 17.2$ mm^2/s obtained from a fit (Figure 3a). However, this law does not capture the behavior at later times, which is better described by a shifted LW law $l_p \sim l_0 + \sqrt{2D_{late} t}$ (this form is motivated by the theory) with $D_{late} \approx 6.3$ mm^2/s and an offset $l_0 \approx 1.1$ cm. We observe that D_{early} in grooved paper is noticeably greater than D_0, while D_{late} is quite close to D_0. This is consistent with the theoretical prediction that initial growth is faster than that in bare paper, while the growth rate at late times is unchanged.

The contact angles of the various faces internal to the groove are difficult to measure directly. As noted earlier, we expect $\theta_s < 90°$ and θ_b and θ_f close to 90°. We treat these angles as fit parameters and choose $\theta_s = 60°$ and $\theta_b = \theta_f = 107°$ (this gives $l_c = 1.7$ cm, $t_c = 45$ s, and $\Lambda = 3.9$). With these parameter values, the analytical theory (eq 12) reproduces the experimental wicking dynamics in the grooved channels of various widths (Figure 3a).

It is interesting to note that increasing the width of the groove from 180 to 230 μm decreases the speed of wicking (though it is still faster than bare paper). This observation was

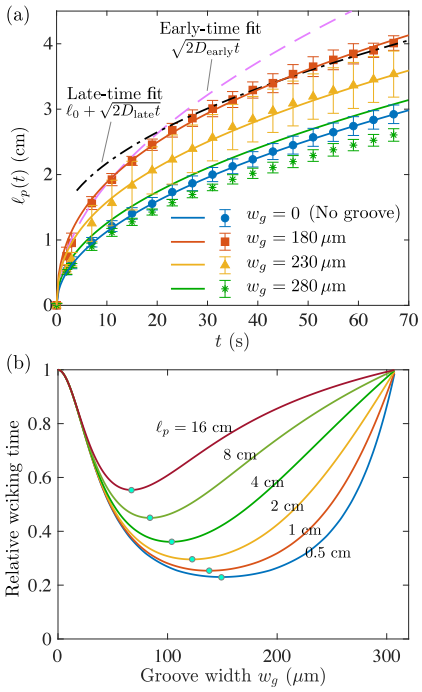

Figure 3. (a) Wicking in paper strips versus groove width showing experiments (Figure 4b "no tape" of Modha et al.;[31] symbols) and model predictions (curves). The model reduces to the LW equation in ungrooved paper, $l_p = \sqrt{2Dt}$. When a groove is introduced, early and late time behaviors are best fit with two different D. Widening the groove from $w_g = 180$ μm to $w_g = 280$ μm leads to slower wicking due to the poorer wettability of wider grooves. (b) Theoretical prediction for the time to wick a length l relative to ungrooved paper as a function of the groove width. The wicking time is minimized at an optimum groove width, marked with circles.

reported previously by Modha et al.[31] but is not explained by area-averaging models,[17,32] which predict that the wicking rate should increase when the relative area of the highly permeable groove is increased. The present theory captures this observed slowdown with an increasing groove width (Figure 3a). This occurs because the front and back surfaces are hydrophobic on average ($\theta_{f,b} > 90°$); therefore, increasing the width of the groove decreases the capillary pressure P_g, lowering both the entrainment factor Λ and the rise height in the groove. Upon further increasing w_g to 280 μm, the wicking is similar to that of the ungrooved paper matrix. While the theory still predicts a slightly faster wicking at this groove width, the experiments of Modha et al.[31] show that it is, in fact, slightly slower than that of the blank paper channel. This is likely the result of tortuous fluid paths through the paper matrix being cut off due to the now reduced width of the paper matrix, leading to a width-dependent permeability k_p of the paper (see the study by Castro et al.[9]), which we do not model here.

When the width of the groove exceeds a critical value $w_g^* = -2d_g \cos\theta/(\cos\theta_f + \cos\theta_b)$, the groove becomes non-wetting (i.e., $P_g = 0$) and no longer participates in the wicking; see eq 13. For $w_g > w_g^*$, the groove splits the paper strip into two, with each half wicking independently of the other, behaving similarly to ungrooved paper. These features imply the existence of an optimum groove width $w_g^{opt} < w_g^*$ that minimizes wicking time. To investigate this optimum theoretically, we consider the same experimental conditions

https://doi.org/10.1021/acs.langmuir.5c04278
Langmuir 2025, 41, 34292−34298

of Figure 3a while systematically varying the groove width. Figure 3b shows the predicted time required for the paper to wick a fixed distance as a function of the groove width, normalized by the time to wick the same distance in ungrooved paper. The wicking is fastest at an optimum width w_g^{opt} that depends on the target wicking distance, with larger distances associated with smaller optimal widths. The optimal width to wick a desired length l can be identified from eq 11 by requiring that (after re-dimensionalizing variables) $dt/dw_g = 0$. Due to the complicated form of eq 11, the optimum cannot be written down in closed form for a general combination of design parameters. However, for small wicking lengths $l \lesssim l_c$, we find that the optimum width is about $\frac{1}{2}w_g^*$ for grooves of roughly square cross-section [$w_g^* = O(d_g)$] and about $\frac{2}{3}w_g^*$ for wider grooves ($w_g^* \gg d_g$). Grooves that are wider than this optimum lead to smaller P_g and thus Λ, whereas narrower grooves offer greater resistance to flow. At larger target wicking lengths, the main effect of the groove is to provide the paper with a source of fluid at a distance $P_g/(\rho g \sin\alpha)$ from the reservoir, as discussed earlier. Since the increased resistance of the groove does not influence the dynamics at late times, the optimal groove width is shifted to smaller values (longer capillary lengths) for longer target wicking lengths, as seen in Figure 3b.

For the experimental parameters considered in Figure 3, the predicted optimum groove width is below 150 μm. Although the experiments make the existence of an optimum clear (the wicking rate increases and then decreases with an increasing groove width), the narrowest groove reported by Modha et al.[31] is 180 μm wide; therefore, we are unable to directly validate the predicted location of the optimum. This remains a task for future work and indicates opportunities for flow control with geometrical surface modifications.

Multiple Grooves. The theory also captures wicking with multiple parallel grooves. We compare again to experiments of Modha et al.,[31] where multiple identical parallel grooves (180 μm wide) with uniform spacing were etched in a paper strip 6 mm wide. Figure 4 plots the time to wick at a distance of 4 cm, showing experiments (symbols) and theory (curves). Increasing the number of grooves increases the rate of wicking. As before, we used the experiment with ungrooved paper to determine the LW mobility, D_0. We then apply the theory "per groove" by interpreting w_p in the theory as the total width of the paper strip divided by the number of grooves. Using $\theta_f = \theta_b = 98°$ as a free parameter (other model parameters are unchanged from before), the theory (eq 12) quantitatively recovers the dependence of wicking time on the number of grooves. We apply the same procedure for paper whose front and back faces are treated with Uline S-423 Industrial Tape (Uline, Pleasant Prairie, WI, U.S.A.), once more finding good agreement with experiments, this time with $\theta_f = \theta_b = 90°$. By contrast, using an area-averaged LW description with an effective pore size $r_{eff} = (A_p r + A_g\sqrt{k_g/8})/(A_p + A_g)$ (dashed curve in Figure 4) in the spirit of previous studies of multi-ply paper-based devices[17] underpredicts the wicking time by an order of magnitude.

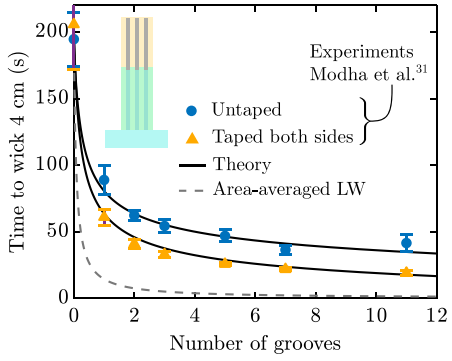

Figure 4. Time required to wick 4 cm as a function of the number of grooves, showing the experiments of Modha et al.[31] and the present model (solid curve). The dashed curve is the prediction of an area-averaged LW model.

CONCLUSION

Engineering surface grooves on paper can have a profound effect on liquid imbibition. Here, we have developed a model based on fundamental principles that predicts the imbibed length as a function of time in terms of interfacial and geometric properties. The model leads to an analytical theory that generalizes the Lucas–Washburn law of multiscale porous media with gravity, controlled by a key dimensionless parameter Λ that characterizes the ratio of fluxes in the groove and the porous paper matrix. The theory is shown to reproduce previously reported experimental studies of vertical imbibition in a grooved channel. A key finding is that gravity plays an important role in the dynamics, as it may be important in the groove, even though it has a negligible influence as a force in the pores of the paper matrix. We also rationalize the observation that increasing the groove width can decrease the rate of wicking and attribute it to the combination of (i) reduced capillary pressure for wider grooves and (ii) the stronger influence of gravity in wider grooves. We predict that the transport is maximally enhanced by a groove with an optimum width that trades off these effects. Finally, we show that the theory captures equally well the imbibition of fluid through paper strips with multiple parallel grooves.

The present work provides a rigorous and quantitatively accurate framework by which to analyze fluid transport in paper channels with modifications to the surface geometry. The model predictions have simple analytical forms; therefore, we envision it to be a useful tool for the design and optimization of paper-based microfluidic devices seeking precise flow control. A prediction of the theory that could be tested in future work is that a downward sloped groove can lead to linear wicking. It would be interesting to realize this behavior in a practical paper-based device. The ideas laid out here may be adapted to more complex configurations involving the exchange of fluid between groove or pore networks with different wettabilities, geometries, and topologies.

AUTHOR INFORMATION

Corresponding Authors

Bhargav Rallabandi − *Department of Mechanical Engineering, University of California, Riverside, Riverside, California 92521, United States;* orcid.org/0000-0002-7733-8742; Email: bhargav@engr.ucr.edu

Hideaki Tsutsui − *Department of Mechanical Engineering, University of California, Riverside, Riverside, California 92521, United States*; Email: tsutsui@ucr.edu

https://doi.org/10.1021/acs.langmuir.5c04278
Langmuir 2025, 41, 34292−34298

Authors

Sidharth Modha − *Department of Bioengineering, University of California, Riverside, Riverside, California 92521, United States*

Brent Kalish − *Department of Mechanical Engineering, University of California, Riverside, Riverside, California 92521, United States*

Complete contact information is available at: https://pubs.acs.org/10.1021/acs.langmuir.5c04278

Notes

The authors declare no competing financial interest.

■ ACKNOWLEDGMENTS

The authors are grateful for support through Award 68257-ND9 from the Petroleum Research Fund of the American Chemical Society.

■ REFERENCES

(1) Martinez, A. W.; Phillips, S. T.; Butte, M. J.; Whitesides, G. M. Patterned paper as a platform for inexpensive, low-volume, portable bioassays. *Angew. Chem.* **2007**, *119*, 1340−1342.

(2) Noviana, E.; Ozer, T.; Carrell, C. S.; Link, J. S.; McMahon, C.; Jang, I.; Henry, C. S. Microfluidic Paper-Based Analytical Devices: From Design to Applications. *Chem. Rev.* **2021**, *121*, 11835−11885.

(3) Modha, S.; Castro, C.; Tsutsui, H. Recent developments in flow modeling and fluid control for paper-based microfluidic biosensors. *Biosens. Bioelectron.* **2021**, *178*, 113026.

(4) Cate, D. M.; Dungchai, W.; Cunningham, J. C.; Volckens, J.; Henry, C. S. Simple, distance-based measurement for paper analytical devices. *Lab Chip* **2013**, *13*, 2397−2404.

(5) Fu, H.; Song, P.; Wu, Q.; Zhao, C.; Pan, P.; Li, X.; Li-Jessen, N. Y. K.; Liu, X. A paper-based microfluidic platform with shape-memory-polymer-actuated fluid valves for automated multi-step immunoassays. *Microsyst. Nanoeng.* **2019**, *5*, 50.

(6) Washburn, E. W. The dynamics of capillary flow. *Phys. Rev.* **1921**, *17*, 273.

(7) Fries, N.; Odic, K.; Conrath, M.; Dreyer, M. The effect of evaporation on the wicking of liquids into a metallic weave. *J. Colloid Interface Sci.* **2008**, *321*, 118−129.

(8) Jahanshahi-Anbuhi, S.; Henry, A.; Leung, V.; Sicard, C.; Pennings, K.; Pelton, R.; Brennan, J. D.; Filipe, C. D. based microfluidics with an erodible polymeric bridge giving controlled release and timed flow shutoff. *Lab Chip* **2014**, *14*, 229−236.

(9) Castro, C.; Rosillo, C.; Tsutsui, H. Characterizing effects of humidity and channel size on imbibition in paper-based microfluidic channels. *Microfluid. Nanofluid.* **2017**, *21*, 21.

(10) Mendez, S.; Fenton, E. M.; Gallegos, G. R.; Petsev, D. N.; Sibbett, S. S.; Stone, H. A.; Zhang, Y.; López, G. P. Imbibition in porous membranes of complex shape: quasi-stationary flow in thin rectangular segments. *Langmuir* **2010**, *26*, 1380−1385.

(11) Fu, E.; Ramsey, S. A.; Kauffman, P.; Lutz, B.; Yager, P. Transport in two-dimensional paper networks. *Microfluid. Nanofluid.* **2011**, *10*, 29−35.

(12) Elizalde, E.; Urteaga, R.; Berli, C. L. Rational design of capillary-driven flows for paper-based microfluidics. *Lab Chip* **2015**, *15*, 2173−2180.

(13) Gorce, J.-B.; Hewitt, I. J.; Vella, D. Capillary imbibition into converging tubes: beating Washburn's law and the optimal imbibition of liquids. *Langmuir* **2016**, *32*, 1560−1567.

(14) Schuchard, D. R.; Berg, J. C. Liquid transport in composite cellulose—superabsorbent fiber networks. *Wood Fiber Sci.* **1991**, *23* (3), 342−357.

(15) Masoodi, R.; Pillai, K. M. Darcy's law-based model for wicking in paper-like swelling porous media. *AIChE J.* **2010**, *56*, 2257−2267.

(16) Diersch, H.-J. G.; Clausnitzer, V.; Myrnyy, V.; Rosati, R.; Schmidt, M.; Beruda, H.; Ehrnsperger, B. J.; Virgilio, R. Modeling unsaturated flow in absorbent swelling porous media: Part 1. Theory. *Transport Porous Med.* **2010**, *83*, 437−464.

(17) Camplisson, C. K.; Schilling, K. M.; Pedrotti, W. L.; Stone, H. A.; Martinez, A. W. Two-ply channels for faster wicking in paper-based microfluidic devices. *Lab Chip* **2015**, *15*, 4461−4466.

(18) Channon, R. B.; Nguyen, M. P.; Henry, C. S.; Dandy, D. S. Multilayered microfluidic paper-based devices: characterization, modeling, and perspectives. *Anal. Chem.* **2019**, *91*, 8966−8972.

(19) Schaumburg, F.; Berli, C. L. A. Assessing the rapid flow in multilayer paper-based microfluidic devices. *Microfluid. Nanofluid.* **2019**, *23* (8), 98.

(20) He, G.-Y.; Wang, Y.-C.; Tsao, H.-K.; Sheng, Y.-J. Wicking dynamics of two-ply channels in porous medium-based microfluidic devices. *Phys. Fluids* **2024**, *36* (6), 062115.

(21) Songok, J.; Toivakka, M. Modelling of capillary-driven flow for closed paper-based microfluidic channels. *J. Micromech. Microeng.* **2017**, *27*, 065001.

(22) Kalish, B.; Tan, M. K.; Tsutsui, H. Modifying wicking speeds in paper-based microfluidic devices by laser-etching. *Micromachines* **2020**, *11*, 773.

(23) He, G.-Y.; Tsao, H.-K.; Sheng, Y.-J. Enhanced wicking dynamics of paper-based microfluidics by a nonporous wall. *Phys. Fluids* **2025**, *37* (2), 022034.

(24) Ruiz-Gutiérrez, É.; Armstrong, S.; Lévêque, S.; Michel, C.; Pagonabarraga, I.; Wells, G. G.; Hernández-Machado, A.; Ledesma-Aguilar, R. The long cross-over dynamics of capillary imbibition. *J. Fluid Mech.* **2022**, *939*, A39.

(25) Kolliopoulos, P.; Jochem, K. S.; Lade Jr, R. K.; Francis, L. F.; Kumar, S. Capillary flow with evaporation in open rectangular microchannels. *Langmuir* **2019**, *35*, 8131−8143.

(26) Kolliopoulos, P.; Kumar, S. Capillary flow of liquids in open microchannels: overview and recent advances. *npj Microgravity* **2021**, *7*, 51.

(27) Steinik, C.; Picchi, D.; Lavalle, G.; Poesio, P. Capillary imbibition of shear-thinning fluids: From Lucas-Washburn to oscillatory regimes. *Phys. Rev. Fluids* **2024**, *9*, 023305.

(28) Salama, A. Investigation of the imbibition/drainage of two immiscible fluids in capillaries with arbitrary axisymmetric cross-sections: a generalized model. *J. Fluid Mech.* **2022**, *947*, A12.

(29) Giokas, D. L.; Tsogas, G. Z.; Vlessidis, A. G. Programming fluid transport in paper-based microfluidic devices using razor-crafted open channels. *Anal. Chem.* **2014**, *86*, 6202−6207.

(30) Liu, Q.; Xu, C.; Liang, H. Laser carved micro-crack channels in paper-based dilution devices. *Talanta* **2017**, *175*, 289−296.

(31) Modha, S.; Shen, Y.; Chamouni, H.; Mulchandani, A.; Tsutsui, H. Laser-etched grooves for rapid fluid delivery for a paper-based chemiresistive biosensor. *Biosens. Bioelectron.* **2021**, *180*, 113090.

(32) Cummins, B. M.; Chinthapatla, R.; Ligler, F. S.; Walker, G. M. Time-dependent model for fluid flow in porous materials with multiple pore sizes. *Anal. Chem.* **2017**, *89*, 4377−4381.

(33) Mortensen, N. A.; Okkels, F.; Bruus, H. Reexamination of Hagen-Poiseuille flow: Shape dependence of the hydraulic resistance in microchannels. *Phys. Rev. E* **2005**, *71*, 057301.

(34) Quéré, D. Wetting and roughness. *Annu. Rev. Mater. Res.* **2008**, *38*, 71−99.